Astronomische Nachrichten

ORIGINAL ARTICLE

High-resolution morphology and surface photometry of KIG 685 and KIG 895 with `ARGOS+LUCI` using the Large Binocular Telescope

Roberto Rampazzo[1] │ **Michela Uslenghi[2]** │ **Iskren Y. Georgiev[3]** │ **Arianna Cattapan[4]** │ **Lourdes Verdes-Montenegro[5]** │ **Marco Bonaglia[6]** │ **Jose Luis Borelli[3]** │ **Lorenzo Busoni[6]** │ **Wolfgang Gäessler[7]** │ **Demetrio Magrin[1]** │ **Antonina Marino[1]** │ **Paola Mazzei[1]** │ **Tommaso Mazzoni[6]** │ **Diethard Peter[3]** │ **Sebastian Rabien[7]** │ **Roberto Ragazzoni[1]** │ **Mathias Rosensteiner[7]**

[1]INAF-Osservatorio Astrofisico di Asiago, Asiago, Italy

[2]INAF-IASF, Milano, Italy

[3]Max-Planck-Institut für Astronomie, Heidelberg, Germany

[4]INAF-Osservatorio Astronomico di Capodimonte, Napoli, Italy

[5]Dep.to Astronomia Extragaláctica Istituto Astrofisica de Andalucía, Granada, Spain

[6]INAF-Osservatorio Astrofisico di Arcetri, Firenze, Italy

[7]Max-Planck-Institut für Extraterrestrische Physik, Garching, Germany

Correspondence
Roberto Rampazzo, Via dell'Osservatorio 8, 36012 Asiago, Vicenza, Italy.
Email: roberto.rampazzo@inaf.it

Abstract

We aim to refine the sample of isolated early-type galaxies in the Analysis of the interstellar Medium of Isolated Galaxies (AMIGA) catalog via high-resolution imaging. Here, we report the result from a pilot study investigating two candidates, KIG 685 and KIG 895, in K-band with the laser guide star and wavefront sensing facility `ARGOS` using the Large Binocular Telescope (`LBT`). Observations, obtained during the commissioning time, achieved a point spread function (PSF) of $\approx 0.25''$. We present the data reduction and the PSF analysis from the best closed-loop exposures to investigate the galaxies' morphological structure, including their nuclear region. We used `PROFILER` for the decomposition of the azimuthal 1D light distribution and `GALFIT` for the 2D analysis, accounting for ARGOS's PSF. KIG 685 was found to be a S0 galaxy and has been modeled with two Sérsic components representing a pseudobulge ($n_{1D} = 2.87 \pm 0.21$, $n_{2D} = 2.29 \pm 0.10$) and a disk ($n_{1D} = 0.95 \pm 0.16$, $n_{2D} = 0.78 \pm 0.10$). Nearly symmetric ring-/shell-like structures emerge after subtracting the `GALFIT` model from the image. KIG 895 shows a clear irregular arm-like structure, in which the northern outer arm is reminiscent of a tail. The galaxy body is a disk, best fitted by a single Sérsic profile ($n_{1D} = 1.22 \pm 0.1$; $n_{2D} = 1.32 \pm 0.12$), that is, KIG 895 is a bulge-less, very late-type spiral. `ARGOS` high-resolution images clearly showed interaction signatures in KIG 895. We suggest that the ring-/shell-like residuals in KIG 685, a bona fide early-type galaxy, point toward a past accretion event.

KEYWORDS

galaxies: individual: (KIG 685, KIG 895), galaxies: interactions, galaxies: photometry, instrumentation: adaptive optics

1 | INTRODUCTION

Early-type galaxies (E + S0 s = ETGs hereafter) are believed to be the by-product of halos merging at high z, although signatures of accretions episodes are found as a function of the richness of the environment (Clemens et al. 2006, 2009). Most of the ETGs inhabit densely populated regions (e.g., the pioneering paper of Dressler 1980) where they are passively evolving (e.g., the mid-infrared analysis by Bressan et al., 2006, of Virgo ETGs). ETGs found in galaxy groups tend to be more active than their cluster counterparts (e.g., Marino et al. 2011a, 2016; Rampazzo et al. 2013, and references therein).

As ETGs tend to be found in galaxy associations (either rich or poor), the expression "isolated early-type galaxies" (iETGs hereafter) may sound like an oxymoron. However, iETGs exist, and studies of single objects, as well as surveys of iETGs, are crucial to understand the effects of interactions on galaxy evolution. Indeed, it is of primary importance to select and to study isolated galaxy samples (e.g., Rampazzo et al. 2016, chapter 5, section 5.3.2). This need has been the driver of catalogues such as Analysis of the interstellar Medium of Isolated Galaxies (AMIGA) (Verdes-Montenegro et al. 2005), a revision of the 1973 *Catalog of Isolated Galaxies* by Karachentseva (1973). The analysis of the AMIGA sample demonstrated a set of galaxies that should not have interacted for at least 3 Gyrs (Verdes-Montenegro et al. 2005; Verley et al. 2007a, 2007b). Although isolation is defined by *spatial criteria*, these criteria in turn imply *temporal*, as well as spatial, isolation. Although a refinement of the existing classifications is still needed based on more detailed studies, iETGs represent a small but significant fraction (~14%) of the AMIGA sample. Very few of them are brighter than $M_B = -21.0$. Fossil ellipticals, that is, a population of galaxies that are the results of the merging of bright group members (e.g., Jones et al. 2003), are not present among iETGs (Sulentic et al. 2006).

The *activity* indicated in ETG members of groups, sometimes not yet virialized, and of loose galaxy associations (i.e., low-density environments, LDEs hereafter) suggests the investigation of the properties of iETGs, inhabitants of extremely poor environments. The *Galaxy Evolution Explorer* (GALEX) (Martin et al. 2005; Morrissey et al. 2007) has widely detected signatures of star formation, indicating a *rejuvenation* of stellar populations, in both the nuclei and outskirts of ETGs in LDE (Marino et al. 2011b; Rampazzo et al. 2007; Salim & Rich 2010; Thilker et al. 2010). Such results are corroborated by mid-infrared nuclear spectroscopy performed by *Spitzer*-IRS, which detected polycyclic aromatic hydrocarbons (Panuzzo et al. 2011; Rampazzo et al. 2013; Vega et al. 2010), that is, signatures of recent star formation activity. A fair upper limit to the contribution of rejuvenation episodes in the last 2 Gyr is ~25% of the total galaxy stellar mass (Annibali et al. 2007), but episodes are typically much less intense than that (few percentages, e.g., Mazzei et al. 2019; Panuzzo et al. 2007; Rampazzo et al. 2013).

Luminosity profiles of ETGs in LDEs are more disk-like in the UV wavelength range than in optical-IR as a consequence of dissipative phenomena in their evolution (Rampazzo et al. 2017). Do iETGs show rejuvenation signatures similar to those seen in ETGs in LDEs? As rejuvenation suggests the occurrence of either interaction or accretion episodes, the basic question is: *how isolated have iETGs been?*

A detailed structural analysis should show signatures of interaction/accretion in iETGs, if any are present, either in the outskirt and/or in their nuclear structure. Deep imaging may indicate the presence of tails (e.g., Duc et al. 2015), ripples, and shells (see the pioneering paper by Malin & Carter 1983). Structural signatures left on the galaxy by its formation history also seem to lurk in the nuclear shape of ETGs. The nature of the cusp-like versus core nuclear shape of the luminosity profile has been vigorously debated for decades. High-resolution, subarcsec observations with the *Hubble Space Telescope* (HST) and high-precision photometric analysis demonstrated the presence of either a cusp or a core shape. In the latter case, the surface brightness becomes shallower as $r \rightarrow 0$ in the nuclear galaxy luminosity profile (Côté et al. 2006; Lauer et al. 1991, 1992, 2002; Turner et al. 2012) with respect to a Sérsic law fit (Sérsic 1963). The presence of either a cusp or a core might distinguish between wet and dry processes, with core nuclei resulting from dry mergers (Kormendy et al. 2009), while cusp results from wet mergers (Khochfar et al. 2011).

The present paper analyses high-resolution images of two galaxies, KIG 685 and KIG 895, performed using *The Advanced Ryleigh Guided Ground layer adaptive Optic System* ARGOS+LUCI (Orban de Xivry et al. 2016; Rabien et al. 2019) using the Large Binocular Telescope (LBT) (Hill et al. 2008) during the commissioning time. The originally larger sample was reduced as a consequence of instrument commissioning needs and bad weather conditions. The targets are part of the iETG sample in the AMIGA catalog (Verdes-Montenegro et al. 2005), specifically designed to spot galaxies with strict isolation criteria (Argudo-Fernández et al. 2013; Verley et al. 2007a, 2007b). Their salient characteristics are collected in Table 1. We considered the classification provided by Fernandez-Lorenzo and AMIGA collaborators (Fernández Lorenzo et al. 2014), HYPERLEDA[1] and Buta

---

[1]http://leda.univ-lyon1.fr

TABLE 1 Galaxy characteristics

KIG	RA J2000 h m s	Dec. J2000 ° ′ ″	Morphology (type) Buta	HyperLeda	F-L+	V_{hel} (km s^{-1})	D (Mpc)	M_B
685	15 30 15.2	56 49 56	E0$^+$:pec (-4)	E (-3.9 ± 2.4)	E/S0 (-3.0 ± 1.5)	$15{,}383 \pm 150$	205.8	-20.89
895	21 00 56.0	10 19 25	SAbc: (4.5)	Sbc (4.4 ± 3.0)	S0/a (0 ± 1.5)	$4{,}828 \pm 17$	65.7	-18.91

Note: Classifications are from the Buta et al. (2019), `HyperLeda` (col. 5), and Fernández Lorenzo et al. (2012) (F-L+ col. 6). The heliocentric velocity (col. 7) is from `NED`. The distance (col. 8) is provided in the Analysis of the Interstellar Medium of Isolated Galaxies (AMIGA) catalog (Verdes-Montenegro et al. 2005). The absolute B-band magnitude in column 9 is derived from the observed, extinction-corrected magnitude, 15.63 ± 0.32 mag. (0.05 mag. Extinc.) and $B_T = 15.18 \pm 0.41$ mag. (0.34 mag. Extinc.) for KIG 685 and KIG 895, respectively, from `HyperLeda`.

et al. (2019). KIG 685 is considered an elliptical by all three classifications, while KIG 895 has an uncertain classification: it is a spiral for Buta et al. (2019) and `HyperLeda` and a late S0/a for Fernández Lorenzo et al. (2014). The large uncertainty in the classification, based on SDSS images, needs to be resolved via high spatial resolution images. Their heliocentric velocity and the distance (Table 1), computed considering $H_0 = 75$ km s^{-1} Mpc^{-1}, are obtained from Fernández Lorenzo et al. (2014). Their absolute B-band magnitudes, corrected for Galactic extinction, differ by ≈ 2 magnitudes.

These iETGs have been observed in K-band during two distinct runs of the `ARGOS+LUCI` instrument commissioning phase (see Table 2). The nominal `ARGOS+LUCI` point spread function (PSF)-FWHM is $\simeq 0.25''$ in K-band and the `LUCI` $4' \times 4'$ field of view (FoV hereafter) largely accommodates our galaxies. Galaxies are selected in order to have a guide plus tip-tilt stars in the field necessary for fruitful observations. Neither of the galaxies observed had prior subarcsec-resolution images. High-resolution exposures allow us (a) to improve their morphological classification and (b) to quantitatively describe their light distribution from the inner regions, including a core versus cusp-like classification of their nucleus, down to their outskirts. We performed the analysis of both the azimuthally averaged surface brightness profile and of the 2D galaxy light distribution, illustrating the interpretation behind the construction of the adopted multicomponent decomposition. We discussed the shape of the residual light distribution after model subtraction from the original image in light of the current literature.

The paper is organized as follows. In § 2, we present the `ARGOS+LUCI` instrument and characterize the observations performed at `LBT`. § 2.1 describes the data reduction method and the field analysis. In this section, we illustrate how the *scientific* frames of each galaxy have been assembled, selecting the best exposures in the stack on the basis of the PSF (see also Rabien et al. 2019). We use a composite, Gaussian plus a Moffat, PSF to describe geometric distortions in the `ARGOS+LUCI` FoV, showing

TABLE 2 Observations in K-band

KIG	Total exp. time (s)	Date	Zero point (mag)
685	945 (3.00 × 315)	March 14, 2017	25.02 ± 0.05
895	673 (2.55 × 264)	October 22, 2016	25.25 ± 0.05

that they do not affect our study. In § 2.2, we discuss how the adoption of a simple Moffat model for the PSF for the light profile decomposition will recover accurate and seeing-free parameters using the Sérsic law. In § 2.3, we present the data reduction performed for obtaining the light distribution and the geometric structure of the galaxies. We describe the programs used for the 1D and 2D light profile decomposition. Results are summarized in § 3 and discussed in § 4 to understand the nature and the evolutionary paths of our galaxies.

2 | OBSERVATIONS AND REDUCTION

`ARGOS` is the Advanced Rayleigh-guided Ground layer adaptive Optics System (Rabien et al. 2019) for the `LBT` at Mount Graham (AZ). By sensing the ground-layer turbulence from three Rayleigh laser guide stars (LGS) on a constellation of $2'$ radius, and focused at 12 km above the telescope, it delivers an improvement by a factor ≈ 2 in FWHM over the $4' \times 4'$ FoV of both `LUCI 1` and `LUCI 2` cameras (Seifert et al. 2003). `LUCI 1` and `LUCI 2` are the two near-infrared wide-field imagers and multiobject spectrographs whose capability and efficiency will be boosted by the increased resolution and encircled energy. The pixel scale of `ARGOS` combined with `LUCI` is $0.118'' \times 0.118''$.

To correct the ground layer turbulence, `ARGOS` uses three green ($5320 \, Å$) light lasers focused at an altitude of 12 km (LGS). A natural guide star (NGS) is used for AO tip-tilt sensing and telescope guiding during the whole observation. Its magnitude should be brighter than $R = 16$ mag and should be located within $2' \times 3'$ field that can be

reached by the First Light Adaptive Optics (FLAO) stage. The NGS requirement reduces the number of iETGs that we can observe with ARGOS.

Table 2 reports the details of the observations. Considering that we are dealing with extended objects, we select the dithering box to be at least two times the radius at $\mu_B = 25\,\mathrm{mag\,arcsec}^{-2}$ of our scientific targets. We calculated it from the value of the log d_{25} diameter tabulated in HyperLeda. The radii are $19.82''$ and $4.35''$ for KIG 685 and KIG 895, respectively. Single exposures have been dithered by $40'' \times 40''$, that is, between 2 and 10 times the radius given above. In order to have an optimal sky subtraction, our present experience suggests that the dithering box should be as large as possible considering the radius of the scientific target and the presence of possible nearby bright stars, including the nearby AO tip-tilt star.

The total exposure has been split into several exposures of about 3 s DIT (see Table 2), primarily to avoid saturation of the galaxy nuclei.

2.1 | Data reduction and field analysis

Each image in the stack has been dark subtracted and flat-fielded. The frames, corrected only for the flat field and dark, have been preliminarily coadded after recentering, and the image obtained has been used to produce a mask of the sources. The mask, with an appropriate offset, has been applied to each single frame before using them to build the average sky. This procedure limits the appearance of artifacts around the galaxies, and it is crucial to demonstrate low surface brightness features.

Blocks of 20 min have been considered for sky correction. This time length has been chosen as a compromise between characterizing shorter time scales and collecting enough statistics despite the masking of sources. In the case of KIG 685, as the region including the target and the nearby (bright) guide star is close to the dithering amplitude, we consider the full dataset to characterize the sky in any position. The average sky image is shown in Figure 1 (top panels). In this way, the information about the variation of the temporal distribution of the sky during the night is lost. To check if this approach was appropriate, we studied the dependence of the sky level on time for several boxes in different positions of the frame to check if the spatial distribution was changing. The ratio between different boxes is nearly constant in a large central area, where the galaxy is located. For boxes selected at the edges of the frame, where artifacts (likely due to scattered light inside the instrument or other instrumental effects) are present, the behavior is different. As these artifacts do not influence the area where the galaxy is located, we scaled the single sky matrix evaluated using the full dataset of

the sky level computed in the central area of each single image to be corrected. For each frame of KIG 895 instead, the sky matrix closest in time has been scaled to the sky median level (computed in the CCD area where the galaxy is located) of the image before the subtraction.

The sky-corrected, dithered images were finally stacked after having been registered using the IRAF[2] GEOMAP and GEOTRAN routines, using as a reference 27 sources for KIG 685 and 77 sources for KIG 895. The full ARGOS+LUCI FoV of KIG 685 and KIG 895 is shown in the mid and bottom left panels of Figure 1, respectively. The results of the sky subtraction are shown in the mid and bottom right panels of the same figure. Signatures of a nonoptimal sky subtraction are still visible at the frame edge where stray light from the telescope structure is apparent. However, close to the galaxies, the residual sky patterns are negligible as shown in Figure 1 for both galaxies.

The ARGOS PSF is well modeled by a Gaussian plus a Moffat composite function. This PSF model (shown in Figure 2, top panels) has been generated by a set of stars close to our target galaxy. We ensured that these stars were not affected by geometrical distortions. We used this composite PSF both to identify the best closed-loop exposures and to map the geometrical distortions in the ARGOS FoV following Rabien et al. (2019).

In order to select the best frames in the stack, we map the PSF-FWHM of the stars in the entire frame and compute the median across the time. The median for each single, dithered frame varies during the run of KIG 895, while for KIG 685, it is stable for all frames. Figure 2 (mid-left panel) illustrates the results for the stack of frames of the KIG 895 observing run. There are frames for which the PSF-FWHM is significantly higher than the average. This is because the Adaptive Optic loop was open. Indeed, the values of the PSF-FWHM when the loop is closed are, on average, at least two times better, as reported by Orban de Xivry et al. (2016) (see their Figure 4) for the K-band imaging. To ensure the best observing condition, a crucial requirement, we excluded from the scientific analysis those images with PSF-FWHM above 2.3 pxs. This threshold value is shown as a dotted line in the mid panel of Figure 2. At the end of this process, for the scientific analysis of KIG 895, we considered 264 (see Table 2) of 297 images. As clearly shown by the mid-left panel of Figure 2, the vast majority of the set of images consistently stacked has been obtained in the final part of the observation.

We mapped the geometric distortion of the ARGOS FoV using KIG 895 frames. There is a large area where the PSF does not change and has narrow Gaussian FWHM and low ellipticity. In Figure 2 (mid-right panel), the PSF map shows that, in general, the PSF-FWHM and its ellipticity

---

[2]iraf.noao.edu

FIGURE 1 *Top left panel*: Average sky image of KIG 685 obtained from dithered frames illustrating the range of illumination patterns to be corrected for. Sources in each frame have been masked before combining them, and each pixel of the sky image is the median of the frames not masked in that position. The median sky value is 4,759.50 ADU. *Top right panels*: Same image enhancing the range $-40 \leq ADU \leq 20$ (i.e., -0.84% $+0.42\%$): the average distribution along x and y axes shows the patterns in the sky image. The red lines are cuts along the x and y axes crossing the center of the field, and the black lines are the average along the x, y axes. *Mid-left panel*: Final frame of KIG 685 after sky subtraction and coadding of the registered images. *Mid-right panels*: Same image, masking the sources and then smoothing to enhance sky patterns with size >50 pixels in the range $-2 \leq ADU \leq 2$ ($\pm 0.04\%$): the average distribution along x and y axes shows the residual patterns present in the KIG 685 image after the sky subtraction. *Bottom left panel*: Final frame of KIG 895 after sky subtraction and coadding of the registered images. *Bottom right panels*: As mid-right panels for KIG 895. The median sky value is 5,138.0 ADU
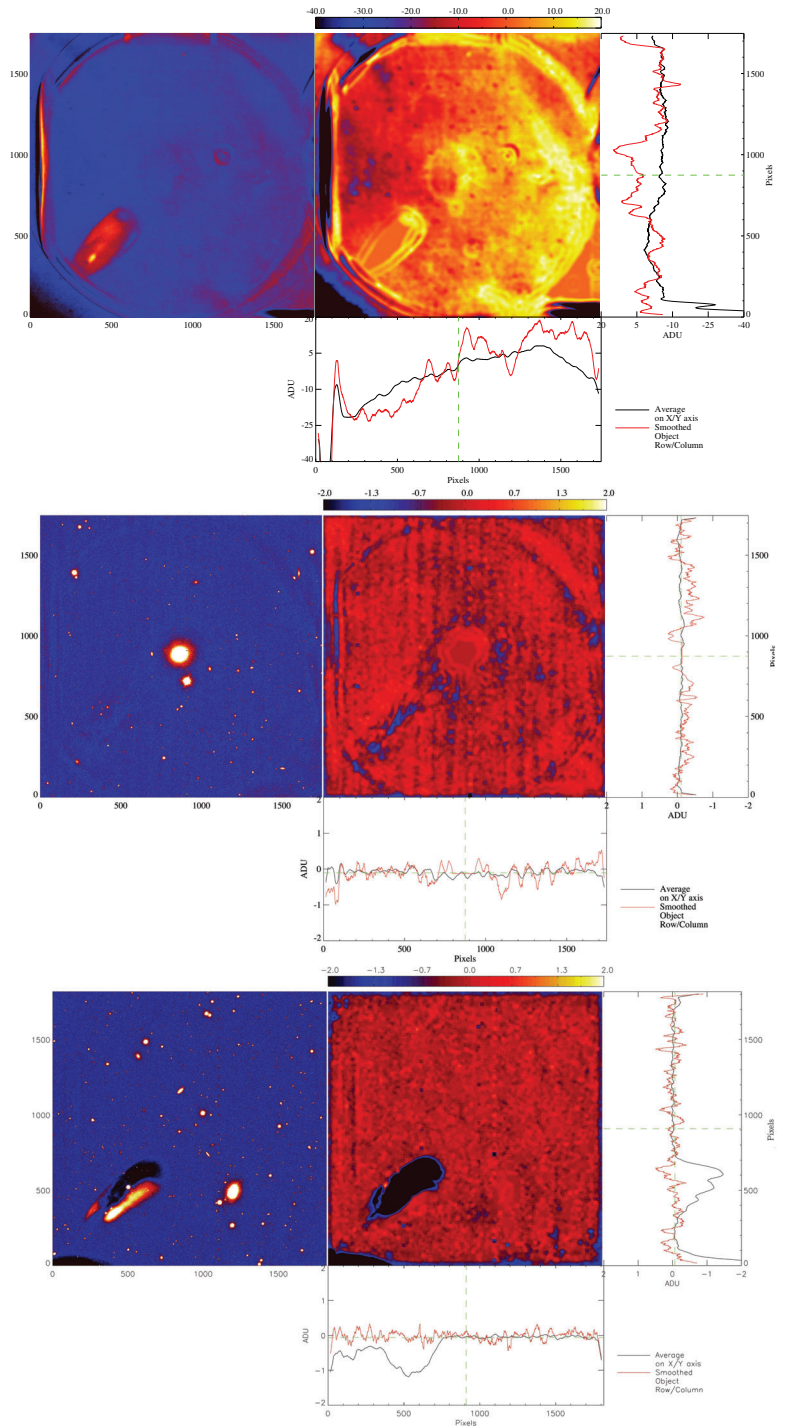
increase toward the detector edge. In the bottom left and right panels, we investigated the spatial variation of the PSF-FWHM and the ellipticity of stars, respectively. The global median Gaussian FWHW is $0.26'' \pm 0.02''$ rms (2.2 pxs); however, the figure shows that the FWHM is $0.24''$ where the galaxy is located (bottom left panel). The bottom right panel of the same figure also shows that the ellipticity of stars is negligible in the area occupied by the galaxy, demonstrating that the galaxy structural analysis is not compromised.

2.2 | PSF adopted for the galaxy light profile decomposition

The study of the PSF is crucial when the galaxy light profile decomposition is performed.

Recent systematic studies of the influence of scattered light on the analysis of faint galaxy outskirts (halos) suggested that PSF should have an extension at least comparable to the size of the galaxy (e.g., Sandin 2014, 2015). Extended PSFs are empirically extracted from the
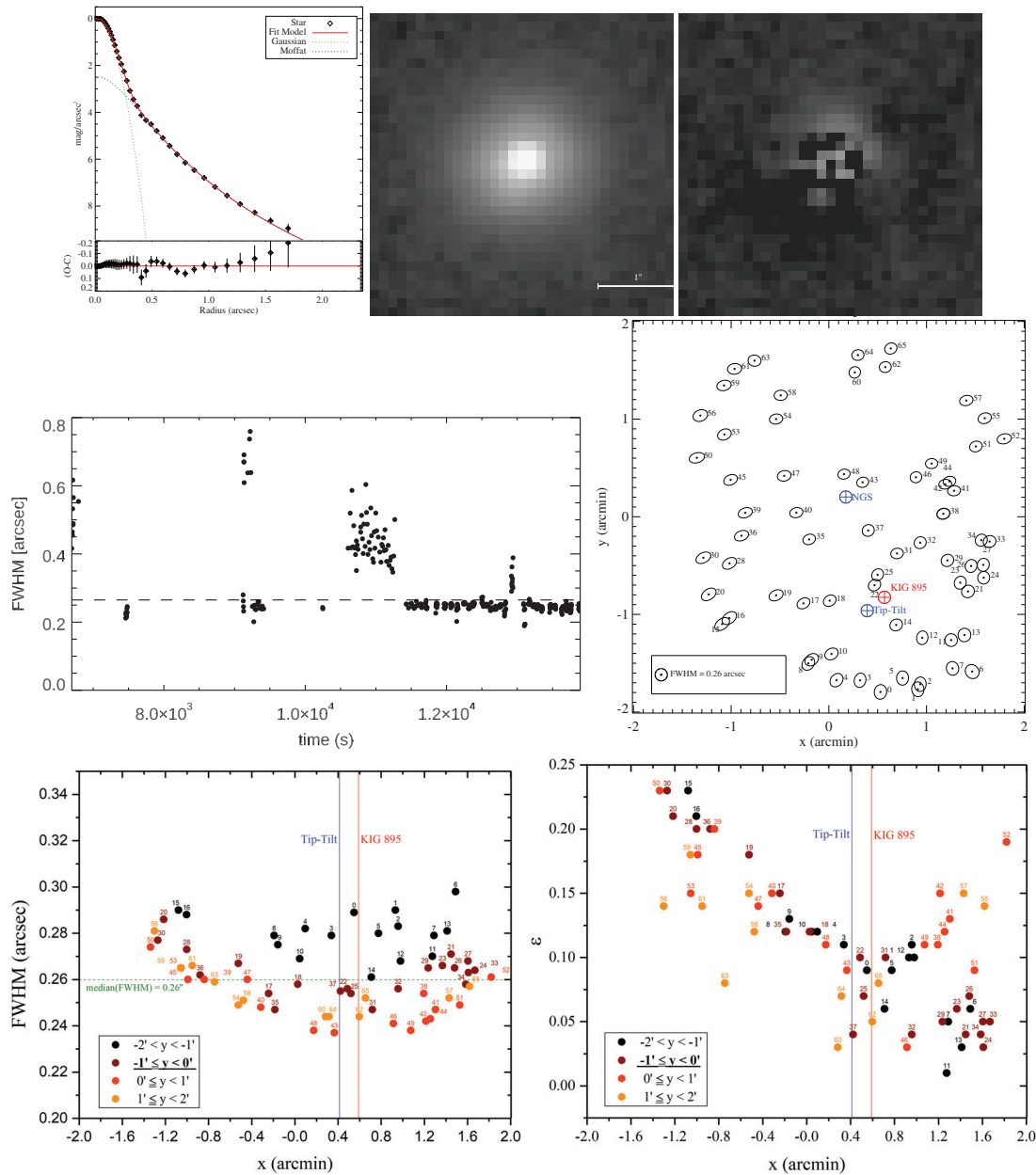
FIGURE 2 Study of the KIG 895 frame. *Top left panel*: Stellar PSF adopted for selecting frames with closed loop. The PSF is best fitted with a composite model (solid line) combining a Gaussian (FWHM = 0.23″) plus a Moffat (β = 2.06 ± 0.02). The PSF has been generated from a set of stars close to the galaxy. *Top mid and left panels*: A star and residuals after the Gaussian + Moffat PSF model subtraction are shown. *Mid-left panel*: PSF-FWHM variation with time in the stack of KIG 895 images. The dotted line indicates the threshold used to select images to be coadded for our scientific use. The threshold is arbitrarily set to 2.3 pxs (0.28″). *Mid-right panel*: 2D map of the Gaussian FWHM variation across the field of view of KIG 895. The semimajor axis and the position angle of the plotted ellipses are proportional to the Gaussian FWHM and provide the direction of its elongation. The positions of the galaxy, of the guide star NGS, and of the tip-tilt star are indicated. FWHM = 0.26″ is the median value. *Bottom right panel*: The distribution of the Gaussian FWHM and (*bottom left panel*) of the stars ellipticity in the four quadrants (see *mid-right panel*) centered on KIG 895

study of bright stars' light profiles obtained in the same band and with the same observing conditions. PSF are wavelength dependent and vary with time (Sandin 2014, 2015). Extended PSFs have been used in very deep *optical* photometry (e.g., Cattapan et al. 2019; Spavone et al. 2018; Trujillo & Fliri 2016).

In the field of KIG 895, there are no very bright stars. The bright star close to KIG 685 cannot be used as its outskirts, that is, where the possible contribution of scattered light can be evaluated, are obviously "perturbed" by the galaxy (Figure 1). Sandin (2015) noticed that, in general, extended PSFs are not yet accurately determined in NIR.
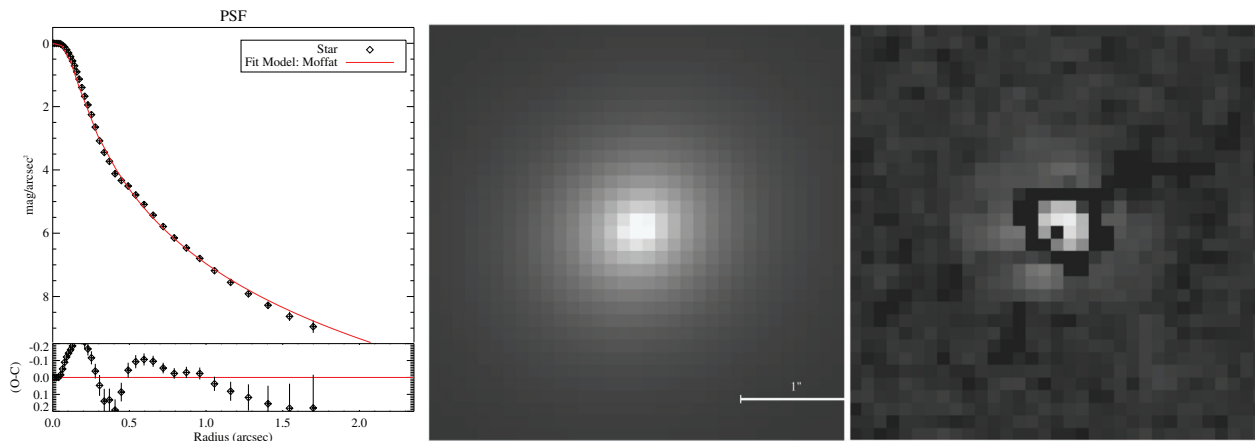
FIGURE 3 Study of the KIG 895 frame. PSF used for the 1D light profile decomposition. *Panels from left to right*: The PSF, best fitted with a Moffat function with $\beta = 1.58 \pm 0.02$; Moffat 2D PSF model, and 2D residuals after model subtraction

On the other hand, the influence of the scattered light on the galaxy outskirts also depends on the compactness of the PSF and on the surface brightness reached. This can be deduced by the accurate deconvolution process applied to the observed data (see detailed discussion by Trujillo & Fliri 2016).

Figure 2 (top left panel) shows that ARGOS PSF has significant *wings*, so we consider a composite, Gaussian + Moffat, PSF model. However, Trujillo et al. (2001) showed that a simple Moffat PSF is a "good option to model narrow PSFs" as the ARGOS one. Figure 3 (right panel) shows the ARGOS PSF best fitted by a simple 2D Moffat function with $\beta = 1.58 \pm 0.02$. The figure also shows that 2D residuals, after model subtraction, are larger than those derived from the Gaussian + Moffat composite PSF model. In the context of the light profile decomposition, we use a simple Moffat model for the ARGOS PSF as it could be easily extended down to the galaxy outskirts by the code adopted for the light profile decomposition (see details in § 2.3).

2.2.1 | Correcting seeing effect

Trujillo et al. (2001) studied the effect of seeing on Sérsic law profiles and provided prescriptions for obtaining seeing-free quantities (e.g., the central intensity, effective radius, the Sérsic n index, and mean effective surface brightness). The main result of the Trujillo et al. (2001) paper is that it is necessary to account for the presence of *wings* in the PSF when the ratio of the effective radius, $r_{\rm eff}$, to the FWHM is small (≤ 2.5). Accounting for the ARGOS FWHM $\approx 0.25''$ and the $r_{\rm eff}$ of our galaxies $\approx 3''$ (see Table 3), the above ratio is about 12, that is, 4.8 times larger than the above limit. Our galaxies are not "small" considering the ARGOS FWHM. *A fortiori*, according Trujillo et al.

(2001), we derived seeing-free parameters from the light profile decomposition adopting a Moffat PSF model for the ARGOS PSF as shown in Figure 3.

2.2.2 | Can we expect significant contribution by scattered light in the galaxy outskirts?

Very deep optical observations (e.g., Cattapan et al. 2019; Spavone et al. 2018; Trujillo & Fliri 2016) reaches surface brightness levels below 29–30 mag arcsec^{-2} in the r SDSS band. The detailed study by Trujillo & Fliri (2016) showed that galaxies may be broadened in their outskirts by the PSF *wings* that scatter light. However, the accurate PSF deconvolution they applied indicates that the broadening takes effect at surface brightness levels fainter than $\mu_{\rm r} = 25$ mag arcsec^{-2} (see their Figure 12). Results similar to Trujillo & Fliri (2016) for the Gran Telescopio de Canarias+OSIRIS camera have been obtained by Spavone et al. (2018) and Cattapan et al. (2019) using VST + OmegaCam at ESO. We need to consider two facts. The first is that the ARGOS PSF is very narrow with respect to the optical PSFs. The PSFs FWHM quoted by the above-mentioned studies are in the range $0.8''$–$1''$ in the best cases, that is, about 3–4 times larger than the ARGOS PSF FWHM. The second is that the surface brightness levels affected by the light scatter are not reached by the present surface photometry, assuming an average $(r - K) \approx 2.9 - 3$ mag for ETGs (Chang et al. 2006) (see § 2.3). Our observations do not reach the galaxy halo regime, where the scattered light effect can be large, as demonstrated by the above-mentioned optical observations.

We conclude that, with the adopted analytic Moffat PSF, extended to the galaxy outskirts by the light decomposition program, we will recover accurate and seeing-free

TABLE 3 Relevant parameters of the galaxies in the K-band

KIG	m_K (mag)	$\langle\epsilon\rangle$	$\langle PA\rangle$ (∘)	n	r_{eff} (arcsec)	Nuclear shape	Peculiar structures
685	11.13 ± 0.15	0.16 ± 0.05	107 ± 4	3.37 ± 0.15	3.34 ± 0.06	∧	Ring-/shell-like
895	11.81 ± 0.10	0.31 ± 0.04	154 ± 8	1.32 ± 0.12	2.79 ± 0.10	…	Bulge-less, irregular arms, tail

Note: Columns 1 and 2 report the galaxy ident and the integrated total magnitude. Columns 3 and 4 show the average ellipticity and position calculated along the entire profile outside the seeing-dominated area evaluated using the `IRAF ELLIPSE` package (Jedrzejewski 1987). The Sérsic index, n (column 5), and the effective radius, r_{eff} (column 6) refer to the best fit with a 2D single Sérsic law obtained from `GALFIT` (Peng et al. 2010). Column 7 provides the nuclear shape. KIG 685 has an excess of luminosity with respect to the best fit with a single 2D Sérsic law (see Figure 5, bottom right panels): we indicate it with a ∧ as for intermediate cusp-like nuclei (e.g., Lauer 2012). KIG 895 has no bulge, and the nuclear region appears to be just underluminous (see Figure 4).

structural parameters from the Sérsic law/s applied (see details in § 2.3). Concerning the periphery of our galaxies, we conclude that, due to the `ARGOS` narrow PSF and the level reached by our surface photometry, the scattered light impact is negligible, if any.

2.3 | Galaxy light profile analysis

Our objective is twofold: to verify the classification and to detail the galaxy structure of iETG candidates by mapping their light distribution from the nucleus down to the galaxy outskirts.

To obtain the photometric and geometric profiles, we adopt the following procedure for the final sky subtracted images. The background and foreground sources have been identified and masked using the adjacent background via the `IRAF` task `IMEDIT` to ensure that they did not significantly affect either the ellipse fitting or the magnitudes calculation. The residual sky background level has been measured well outside the galaxy emission in several areas. Its average value is close to zero as shown in Figure 1.

The center of the galaxy was found using the `IMEXAMINE` task of `IRAF`. Light and geometric profiles are obtained using the `IRAF ELLIPSE` task (Jedrzejewski 1987). `ELLIPSE` was instructed to hold the center position constant, whereas the ellipticity and position angle of the ellipses interpolating the galaxy isophotes were allowed to vary. The `ELLIPSE` output consists of a table providing the azimuthally averaged surface brightness profile, as well as the variation of the ellipticity ϵ; the position angle *PA* and a_4; and the amplitude of the fourth cosine coefficient of the Fourier expansion along the semimajor axis of the ellipses that interpolate the galaxy isophotes. The surface brightness errors are estimated by propagating errors on the isophotal intensity provided by `ELLIPSE`, the residual background, and the zero point.

We adopted the `PROFILER` program (Ciambur 2016) to fit azimuthally averaged surface brightness profiles (1D profile hereafter) as obtained from `ELLIPSE`. This software allows fitting the light profile with a model obtained from a linear combination of analytical functions (e.g.,

Sérsic, core-Sérsic, exponential, Ferrers, etc.), describing the photometric components (e.g., disk, bulge, bar, point-source, etc.), convolved with a selected PSF. The convolution of the model with the adopted PSF is performed in 2D using a Fast-Fourier Transform-based scheme, conserving model total flux and allowing for elliptical models (e.g., Trujillo et al. (2001)). In `PROFILER`, we select a Moffat PSF (see Figure 2 right panel) using our specific FWHM and β parameter (see § 2.2). The program generates the PSF internally to a radial extent to at least match or exceed that of the galaxy profile (see Ciambur 2016). `PROFILER` uses an unweighted least-squares minimization method in units of surface brightness in order to avoid possible bias generated by the high S/N central data. The program, using a least-squares algorithm (Marquardt 1963), minimizes the quantity $\Delta_{rms} = \sqrt{\sum_i (\mu_{data,i} - \mu_{model,i})}$, where i is the radial bin, μ_{data} is the surface brightness profile obtained from `ELLIPSE`, and μ_{model} is the model at one iteration. Δ_{rms} provides the global quality of the fit. Along the semimajor axis a, the residual profile $\mu(a) = \mu_{data}(a) - \mu_{model}(a)$ should scatter about zero, with a scatter level within the luminosity profile errors. Solutions may be reached including one or more components, which, however, should be physically motivated. Ciambur (2016) further suggests avoiding the exclusion of data from the luminosity profile, particularly in the central region (where the S/N is high), and varying the radial extent of the fit to investigate the stability of the selected model and uncertainties in its parameters.

We also performed a 2D image analysis using `GALFIT` (Peng et al. 2010). `GALFIT` has been widely used in analyzing both optical and infrared data (e.g., Meert et al. 2015; Salo et al. 2015). The 2D fitting codes require the uncertainties of the pixels as input. The adopted uncertainty matrix has been generated by `GALFIT` based on the `GAIN` and `RDNOISE` keywords from the header of our images assuming a Poissonian statistics (Peng et al. 2010).

The 1D and 2D approaches provide different advantages/disadvantages (e.g., Ciambur, 2016, and references therein). In the 2D image, modeling all pixels, excluding masked ones, contribute to the fitting process but suffer

from the fact that components have single, fixed values for the ellipticity, position angle, and Fourier moments. In the 1D light profile decomposition, pixels contribute in an azimuthal-average sense and take the geometrical parameter variations of radius into account. In other words, they provide a similar but not necessarily identical description of the galaxy light distribution. In some cases, the 2D approach does not provide a meaningful solution.

We use both approaches to describe the structure of our galaxies. After a visual (re)classification was performed on our high-resolution images, we adopt the following strategy for the decompositions. Both for the 1D and 2D decompositions, we start from the simple models, adding as many *reasonable* physical components as necessary in order to improve the fit. We use, for example, a simple Sérsic component + PSF for ellipticals and a bulge+disk (two Sérsic or one Sérsic plus an exponential function) + PSF for unbarred S0s. We use the geometric information in the `ELLIPSE` output to provide hints about the presence of additional components, for example, twisting, negative, or positive value of Fourier moments. Even a *crude* representation of the light profile, for example, a simple Sérsic law fit, provides useful information and is sometimes the only decomposition that may be compared with the literature.

We used the photometric zero points listed in Table 2 obtained from standard stars observed during the same commissioning night.

In both cases, the `ARGOS+LUCI` observations permit the extension of the surface brightness profile down to $\mu_K \sim 21 - 21.5$ mag arcsec^{-2}. The relevant parameters derived by our K-band photometry are given in Table 3.

3 | RESULTS

In the following subsections, we describe the results of the image analysis performed on the light profiles in order to assess the shape of the light distribution, the galaxy structure, and the presence of possible asymmetries and/or peculiarities. Results summarized in Table 3 refer to the single (2D GALFIT) Sérsic fit of the galaxy luminosity profile. These values are normally used for comparisons with other ETG samples.

3.1 | KIG 685

Figure 4 (top right panel) shows the image of KIG 685 and of the surface brightness levels. We compute the best fit of the galaxy azimuthal light profile obtained from ELLIPSE (top left panel) using PROFILER, adopting a Moffat model

of the PSF as discussed in § 2.2. The best-fit model with a single Sérsic component, with index $n_{1D} = 3.21 \pm 0.15$, is shown in the mid-left panel. This value is typical of E/S0s galaxies (e.g., Ho et al. 2011; Huang et al. 2013; Li et al. 2011, and references therein). The fit, however, is not satisfactory. It shows large residuals, as highlighted by the trend of $\Delta\mu$ (i.e., [O-C]) in the same panel, both in the inner regions and outside, of $\sim 2''$, where deviations are of the order of 0.1 mag arcsec^{-2} and extend along all the light profiles. The residuals hint that additional components are present. This is supported by both the ellipticity, suddenly decreasing from $\epsilon \approx 0.2$ to ≈ 0.1 at $\sim 4,''$ and by the trend of the fourth cosine coefficient, a_4, which switches from negative to positive values at about the same radius, suggesting the presence of a disk. The position angle is quite stable outside the seeing-dominated area. This behavior is typical of an S0 rather than a bona fide elliptical. We then include in the fit a second Sérsic law as shown in the mid-right panel. The fit improves (Δrms decreases), indicating that at least two physically motivated components are realistically present: a bulge or pseudobulge ($n_{1D} = 2.87 \pm 0.21$ lower than the classical r$^{1/4}$ law) and a nearly exponential disk ($n_{1D} = 0.95 \pm 0.16$). The exponential disk is a particular case of the Sérsic law (Sérsic 1963) with $n = 1$. The effect of adding a second component reverberates along all the light profile up to the center. The trend of the ellipticity (ϵ) and the isophotal shape, a_4, start to vary e at $\approx 4''$; however, a_4 reaches the highest values of the "disk-like" regime at about 8–10$''$, where the disk emerges in the two-component fit (see Figure 4, mid-right panel).

We used the results of the 1D fit to configure `GALFIT` and to explore the 2D decomposition, shown in the bottom panel of Figure 4. To account for the 2D PDF, we input a real star whose light profile is shown in the top left panel of Figure 2. The 1D n value is consistent with $n_{2D} = 3.37 \pm 0.15$ obtained from the 2D single Sérsic law fit. Residuals show that the center is not well fitted and display a system of ring-/shell-like structures. In the bottom right panel of Figure 4, we show the residuals after subtracting the 2D `GALFIT` model using two Sérsic laws with $n_{2D} = 2.29 \pm 0.12$ and $n_{2D} = 0.78 \pm 0.10$, as suggested by the 1D approach. Diffuse, concentric, ring-/shell-like residuals are still present but grow fainter and fainter from the center to the outskirts of the galaxy. The nucleus shows an excess of light with respect to the model as seen in the bottom right panel of Figure 4.

The inner ring recalls the band demonstrated in the residuals of NGC 3962, a bona fide E, after a single Sérsic law fit by Salo et al. (2015) (their Figure 13). The authors commented that the consideration of an additional component may fit the profile slightly better. In the present case, there is also an outer concentric ring-/shell-like
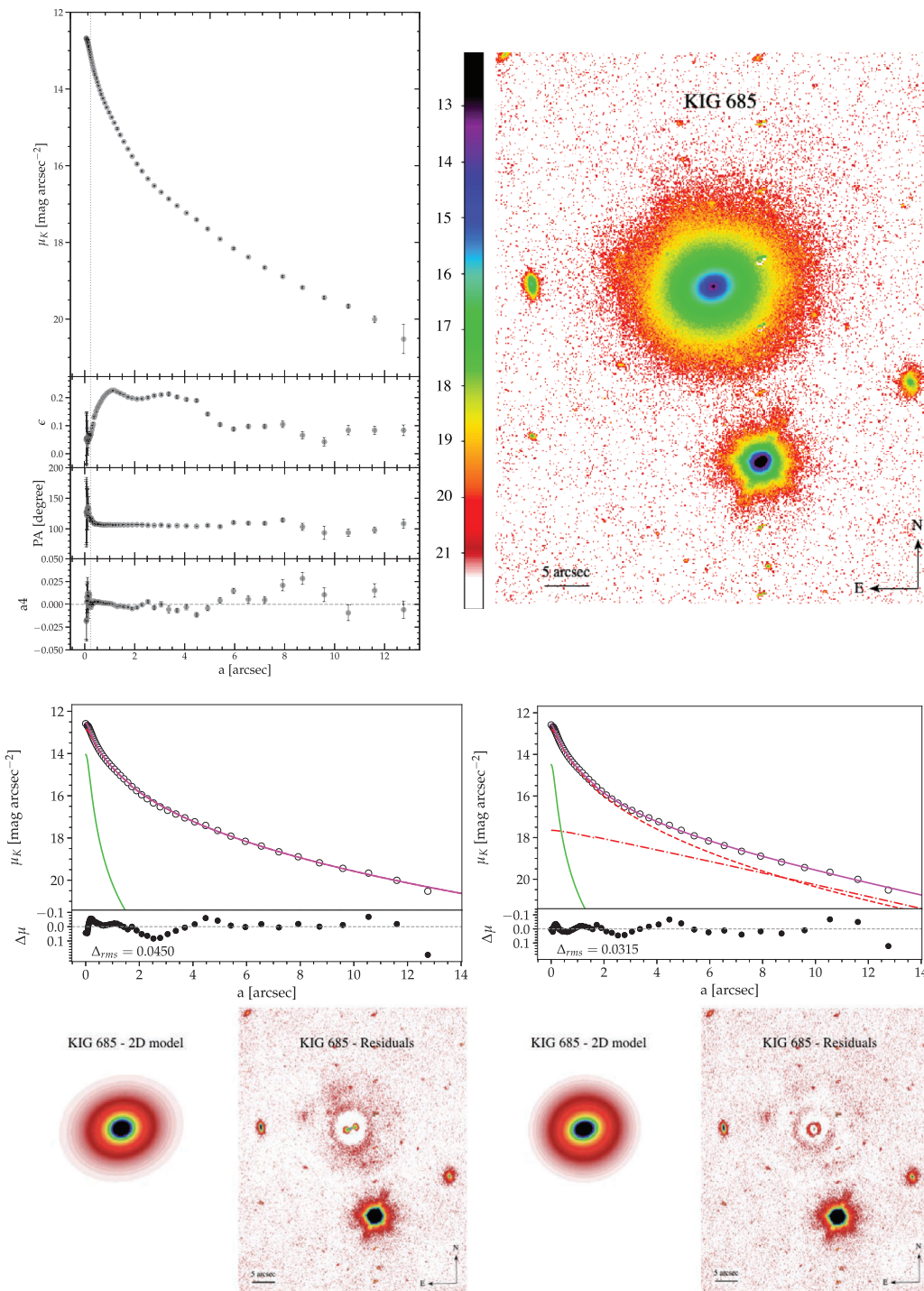
FIGURE 4 KIG 685. *Top left panel*: K-band galaxy light profile and isophote geometry, that is, from top to bottom, the variation of the ellipticity (ϵ), Position Angle (*PA*), and of the forth cosine coefficient (a_4) from ELLIPSE fitting as a function of the galaxy's semimajor axis. The vertical dotted line indicates the area dominated by the seeing (PSF-FWHM = 0.24″). *Top right panel*: K-band image of the galaxy. The surface brightness levels are shown on the right. The double-dounut vertically aligned sequences on the right of the galaxy are ghost images generated by the two close bright stars below KIG 685, due to amplifier electrical cross-talk between the channels of the multiplexer. These ghosts are masked during the surface brightness distribution analysis. *Mid-left panel*: The 1D best fit of the galaxy light profile using PROFILER (Ciambur 2016) is shown. A single Sérsic law $n_{1D} = 3.21 \pm 0.15$, $r_e = 3.12″ \pm 0.10″$ is used + a Moffat PSF (green line, see § 2.2). In the *mid-right panel*), two Sérsic laws $n_{11D} = 2.87″ \pm 0.21$, $r_{e,1} = 2.09″ \pm 0.3″$, $n_{21D} = 0.95 \pm 0.16$, $r_{e,2} = 6.50″ \pm 0.14″$ are fitted. The rms of the best fit obtained is indicated. *Bottom right panel*: The 2D galaxy model of the galaxy light distribution with a single Sérsic (*Bottom left panel*) and two Sérsic functions obtained from GALFIT (Peng et al. 2010) and the correspondent residuals, after the model subtraction, are shown. Values for the 2D decomposition are reported in Table 3 and in the text

component, not indicated in NGC 3962, complicating the case. Shells and ripples are usually asymmetric structures; however, remarkable examples of symmetric shells have been observed (e.g., the shell of NGC 4414 Morales et al. 2018, in their Figure 2). From this analysis, we conclude that the best *physical description* of KIG 685 considers an underlying galaxy structure made of two dominant components—a pseudobulge and a disk—plus ring-/shell-like residual structures. The presence of a wide regular shell system is confirmed by our g and r SDSS band observations of KIG 685 performed with the 4KCCD at the VATT telescope.

The total integrated magnitude we derived from GALFIT is $m_K = 11.13 \pm 0.15$, accounting for the distance given in Table 1; this corresponds to $M_K = -25.43$ mag. HyperLeda provides $m_K = 11.78 \pm 0.13$, and NED provides two total K_s similar values of 11.878 ± 0.057 and 11.651 ± 0.064. The HyperLeda magnitude is computed as the error-weighted average of all the measurements in the K-band, basically from 2MASS. Our K-band total magnitude is brighter (in both KIGs; see § 3.2). We note here the work by Andreon (2002) who suggests that 2MASS magnitudes severely underestimate fluxes, particularly of galaxies in the nearby universe, due to background over-subtraction. However, we did not find new measures to compare with in the *UKIRT Infrared Deep Sky Survey* (UKIDSS) database.

Our values of the average ellipticity and position angle, provided in Table 3, compare well with $\epsilon = 0.11$ and P.A. = 110.6 provided by HyperLeda.

3.2 | KIG 895

The K-band image of KIG 895, shown in Figure 5 (top right panel), shows irregular and wrapped arms embedded in a more extended structure whose average ellipticity is $\epsilon \approx 0.36$. The NW outskirts of the galaxy show an extended arm, reminiscent of a tail, and a remarkable asymmetry with the SE outskirts (see also the 2D residuals in the bottom right panel). All geometrical profiles appear perturbed by the presence of the arm structure. The light profile, shown in Figure 5 (top left panel), extends to $\mu_K \approx 21$ mag arcsec^{-2}.

Using PROFILER, we best fit the light profile with a single Sérsic law with $n_{1D} = 1.22 \pm 0.10$ ($n_{2D} = 1.32 \pm 0.12$ from best fit with GALFIT). No other component is needed to model the *underlying* galaxy structure (see residuals from the 1D best fit shown in top left panel). So, the fit suggests that the underlying structure of KIG 895 is a disk. We emphasized that the system does not show any bulge.

From the integration using GALFIT, the total magnitude is $m_K = 11.81 \pm 0.10$ mag. Assuming the distance in Table 1, we obtained the total integrated absolute magnitude $M_K = -22.28$ mag. The value provided by HyperLeda is $m_K = 12.29 \pm 0.09$, while the 2MASS total magnitude in the K_s band is 12.21 ± 0.096, which are both ∼0.4 magnitudes fainter than our value. As in the case of KIG 685, no value is found in UKIDSS for this object.

Our values of the average ellipticity and position angle, provided in Table 3, agree—within the errors—with $\epsilon = 0.31$ and P.A. = 169.0 provided by HyperLeda.

4 | DISCUSSION

The galaxies examined in this paper inhabit very LDEs. Their degree of isolation is illustrated by Figure 6 in the context of the 114 iETGs selected from the AMIGA sample. Verley et al. (2007b) have revised the isolation criteria of the AMIGA sample by computing the η_K and Q parameters shown in the figure. The parameter η_K is an estimate of the local galaxy number density that considers the distance of the kth nearest neighbor of a similar size to avoid contamination of background galaxies. The farther the kth galaxy is, the smaller the value of η_K, providing a description of the environment of the galaxy considered a primary. However, it is necessary to take into account the mass of the possible perturber/s. The parameter Q is the logarithm of the sum of the tidal strength produced by all possible perturbers in the field: the greater the value, the less isolated from external gravitational forces the galaxy (see the discussion in Jones et al. (2018) on the alternative use of the isolation parameters of Argudo-Fernández et al. (2013)).

Both KIG 685 and KIG 895 are located within the fiducial range in the Q versus η_k plane for isolated galaxies (dashed horizontal and vertical lines in Figure 6). Verley et al. (2007b) showed that pairs, triplets, and compact groups are located outside this area.

Although the sample of galaxies in AMIGA has been widely investigated to exclude the contamination of either interacting or postinteracting objects, high-resolution images may unveil the past history of the galaxies, particularly of ETGs that are widely considered the remnants of interaction/accretion/merging episodes (e.g., recent papers by Eliche-Moral et al. 2018; Mapelli et al. 2015; Mazzei et al. 2014a, 2014b; and references therein). These episodes may leave long-lasting signatures on a galaxy's morphological structure, from the nucleus to the outskirts. Structures such as shells and ripples in ellipticals (Malin & Carter 1983) have long been associated with either minor or major mergers (Dupraz & Combes 1986, 1987; Weil & Hernquist 1993). Recently, Eliche-Moral et al. (2018) and Mazzei et al. (2019) show that some features in S0s, such as
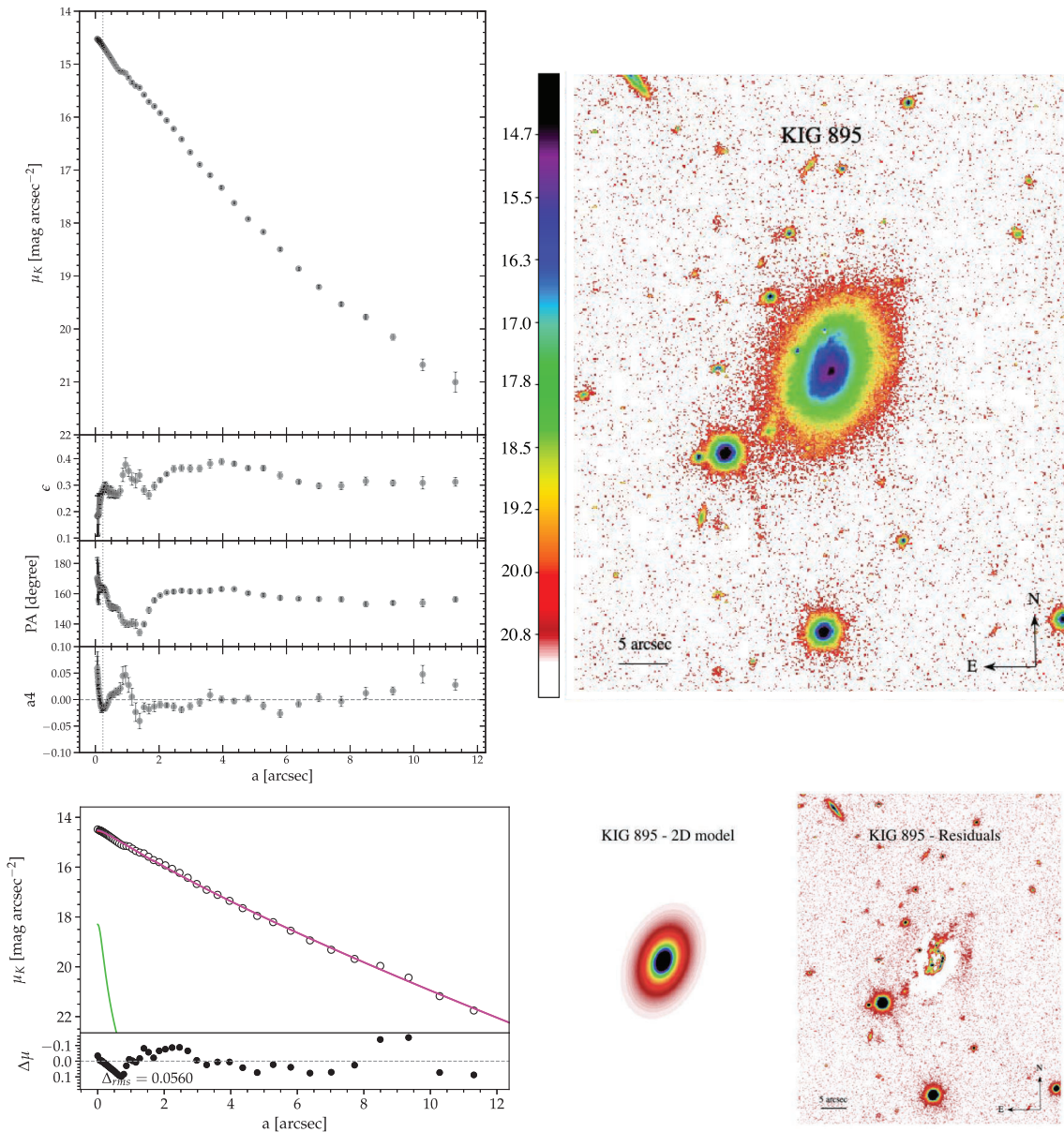
FIGURE 5 KIG 895. *Top left panels*: K-band galaxy light profile and isophote geometry as in Figure 4. *Top right panel*: K-band image of the galaxy. The surface brightness levels are shown on the right. *Bottom right panel*: The light profile is best fitted with PROFILER (Ciambur 2016) by a the PSF (green line, see § 2.2) + a single Sérsic law $n_{1D} = 1.22 \pm 0.10$, $r_e = 2.66'' \pm 0.10''$. The rms of the best fit obtained is also shown. *Bottom right panel*: The 2D model of the galaxy obtained with GALFIT (Peng et al. 2010) using a single 2D Sérsic model with $n_{2D} = 1.32 \pm 0.12$ is shown. Residuals after the model subtraction show an arm-like structure with a tail in N-E part

arm-like structures and rings, may be generated by mergers. In general, it is more common to detect merger relics in S0s that formed via minor mergers than major mergers in a given evolutionary period. On the other hand, the variety of structures demonstrated in S0s, such as bar, lenses, and barlenses, whose frequency is much higher than shells/ripples, has also been interpreted as a result of a more *gentle secular evolution* and/or a transformation of spirals into S0s (e.g., Buta et al. 2010; Laurikainen et al. 2011, 2010).

4.1 | What do our K-band images and light profile analysis tell us in this context?

KIG 685 is classified as a peculiar elliptical (E$^+$0 pec $T = -4$) by Buta et al. (2019) (Table 1), while Fernández Lorenzo et al. (2014) classified it E/S0, that is, slightly later in type ($T = -3$). The total absolute magnitude, adopting the distance reported in Table 1, suggests that the galaxy is located at the bright end of the magnitude distribution of
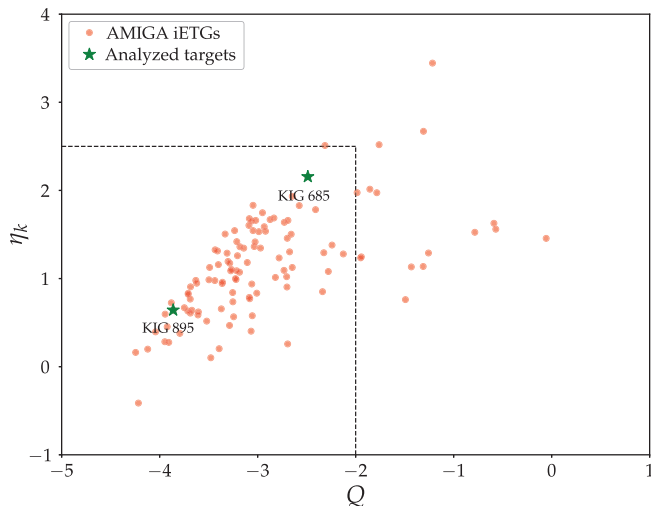
FIGURE 6 Degree of isolation of KIG 685 and KIG 895 (green stars) plotted together with the iETGs (red full dots) in the Analysis of the Interstellar Medium of Isolated Galaxies (AMIGA) sample (see text). The horizontal and vertical dashed lines encloses the fiducial isolated galaxies in the sample (Verley et al. 2007a, 2007b)

ETGs. The best fit of its light distribution suggests the presence of two distinct and physically motivated components: a pseudobulge and an outer disk. The galaxy nucleus is slightly overluminous, that is, cusp-like, with respect to the models. The residuals after the 2D model subtraction show a series of rings-/shell-like structures extending down to the galaxy outskirts, whose intensity decreases from the center to the outskirts. Even if ring-like residuals have been generated by secular evolution, shell-like residuals are explained in a merger framework. Longhetti et al. (1999), from a line-strength indices analysis of ETGs, suggested that shell structures are long-lasting features. In this perspective, KIG 685 may have suffered a merging episode as indicated by the presence of these structures. As in many merger remnants studied by Rothberg & Joseph (2004) (Figure 7), the presence of a cusp-like nucleus, as well as the presence of a disk (see the positive a_4 in the galaxy outskirts), suggests some" wet" merging event in the past.

Our high spatial resolution image of KIG 895 should contribute to the clarification of its uncertain classification ranging from early-type ($T = 0 \pm 1.5$) to spiral SAb_c: ($T = 4.4 \pm 3.0$).

The morphological analysis of 2352 galaxies of Buta et al. (2015) from the *Spitzer* Survey (S^{4}G) showed a subclass they call 3D early-type (3D ETGs). As examples, they discussed 12 cases. These systems have an embedded disk (see their Figure 23) seen under different inclinations in the dust-enshrouded view offered by *Spitzer*. The case of NGC 4384 is of particular relevance. The authors describe the galaxy structure as follows " … The inner part of the

galaxy is a clear SB(rs)dm type with virtually no bulge . . . ." KIG 895 is reminiscent of NGC 4384: both galaxies are bulge less and show inner irregulars arms and a featureless disk in the outer regions, if we exclude the N-W arm that looks like a tail in KIG 895. NGC 4384 has an integrated total magnitude of $M_K = -22.75$ (assuming a distance of 41.1 Mpc). KIG 895 is about half a magnitude fainter. However, the range in magnitude of the 12 3D ETGs in the Buta et al. (2015) is $-25.02 \leq M_K \leq -21.77$ (NGC 5078 and NGC 3377, respectively), assuming distances (Virgo+Great Attractor+Shapley) from NED. Disk-like *Es* have long been known (e.g., Bender et al. 1989; Capaccioli et al. 1990; Jedrzejewski 1987) and are thought to populate one end of the disc-to-bulge sequence including S0s and spiral galaxies (e.g., Cappellari 2016).

On the other hand, the lack of a bulge and its irregular arms-like structure suggests that KIG 895 is a late-type spiral, later in type than SAb_c:. Several measures indicate that, in KIG 895, both atomic and molecular gas are present. Jones et al. (2018) reported log $M(\text{HI}) = 9.30 \pm 0.12 \, M_\odot$ (adopted distance 76.1 Mpc) with a corrected velocity width at the 50% level of 246 km s^{-1}. CO observations by Lisenfeld et al. (2011) demonstrated the presence of molecular hydrogen: log $M(\text{H2}) = 8.29 \, M_\odot$. Lisenfeld et al. (2007) also detected a significant Far Infrared emission, log $L_{\text{FIR}}/L_\odot = 9.6$ (their adopted distance was 60.2 Mpc). All these values are compatible with a spiral classification. The presence of a wide irregular spiral structure, highlighted by our K-band analysis (Figure 5), is not compatible with an ETG classification. Our project aims at characterizing the (full) sample of iETGs with respect to both *normal* ETGs located in different environments and ongoing or recent merger remnants. The first sample is quite difficult to assemble as a significant fraction of ETGs show merging/interaction signatures, particularly when seen through deep optical imaging (e.g., Duc et al. 2011; Spavone et al. 2018 and references therein). This difficulty is reinforced when the ETGs, located in LDEs, are seen in the HI window (Serra et al. 2012), in the Far UV range (see e.g. Marino et al. 2011b; Rampazzo et al. 2007, 2017, 2018), and in MIR (e.g., Rampazzo et al. 2013, 2014, and references therein). Indeed, HI shows clear distortions in many objects; FUV and MIR observations indicate residual star formation.

We consider two comparison samples of ETGs observed in K-band: the *Spheroids Panchromatic Investigation in Different Environmental Regions (SPIDER))* survey (La Barbera et al. 2010) and the study of merging remnants by Rothberg & Joseph (2004).

The *SPIDER* sample investigated 5080 bright ($M_r < -20$) ETGs in the redshift range of 0.05–0.095 in different environments in the *griz*YJHK wavebands. The MIR magnitudes are derived from the UKIRT Infrared
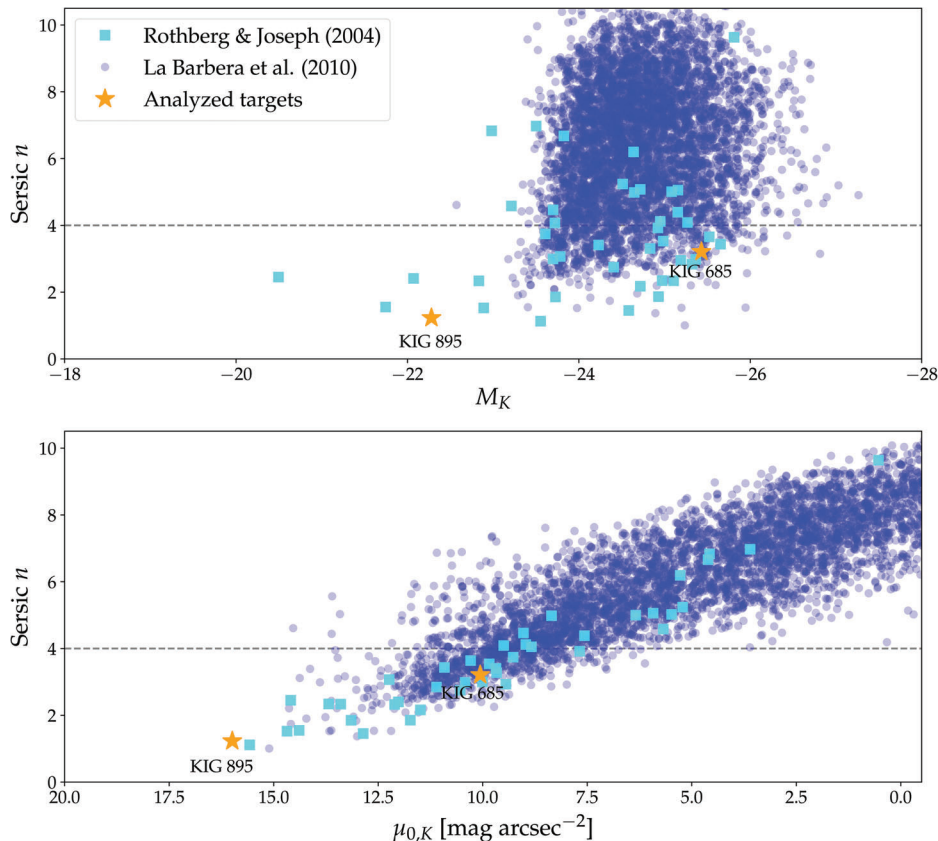
FIGURE 7 *Top panel*: Absolute K-band magnitude and (*Bottom panel*) central surface brightness $\mu_{0,K}$ versus Sérsic index n for merging galaxies in Rothberg & Joseph (2004) (cyan open squares) and ETGs in the *SPIDER* survey located in different environments (La Barbera et al. 2010) (blue full dots). R + J (2004) sample is composed of mergers, ULIRG/LIRG mergers, and shell ellipticals. KIG 685 and KIG 895 are indicated with full yellow stars. The dashed line in both panels indicates the "classical" $r^{1/4}$ de Vaucouleurs law (de Vaucouleurs 1953)

Deep Sky Survey-Large Area Survey (UKIDSS-LAS). The sample we used here is composed of 4,574 ETGs as galaxies with an error in r_e larger than 70% have been removed (La Barbera, private communication). Magnitudes have been *k-corrected* to $z = 0$ and corrected for dimming. ETGs in the *SPIDER* sample may show significant residuals of different shapes (see their Figures 6 and 7) after a Sérsic model has been subtracted from the original image. This suggests that the sample includes a large variety of ETGs from merger remnants to more relaxed objects.

Rothberg & Joseph (2004) investigated the K-band photometric properties of 51 nearby candidate merger remnants, including shell ellipticals and ULIG/LIRG galaxies, to assess the viability of spiral–spiral mergers to produce bona fide elliptical galaxies. The analysis has been conducted with a good seeing FWHM $0.5'' \leq FWHM \leq 1.1''$. They found that the structure of the remnants had undergone a violent relaxation, so their luminosity profiles are comparable to that of an elliptical as 42 of 51 candidate merger remnants have a luminosity profile compatible with a de Vaucouleurs (1953) $r^{1\epsilon 4}$. Moreover, 16 of 51 mergers show evidence of an excess of light in their inner regions. This has been considered evidence either of a wet accretion event, giving rise to star formation episodes in the center of the galaxy, or of *dry* accreted galaxies, which already possessed cusp-like nuclei. Most of the mergers show evidence of disk-like isophotes, that is, the amplitude

of the fourth cosine coefficient of the Fourier expansion of isophotal fit is positive ($a_4 > 0$).

Figure 7 shows that merger remnants (cyan squares) share many characteristics of a large sample of ETGs (blue full dots). In particular, they show a very weak correlation between M_K and the Sérsic index n, such as ETGs, and a stronger correlation between the K-band central surface brightness, $\mu_{0,K}$, and Sérsic index, that is, the light is more centrally concentrated than expected. Together with KIG 685, in Figure 7, we also consider KIG 895, although we proposed a late spiral classification. Its high degree of isolation, the presence of the northern tail, the irregular arms, and asymmetries make the galaxy a possible merger candidate that would fit well in the Rothberg & Joseph (2004) sample. Similar morphologies are indeed found in the that sample, for example, UGC 4079, NGC 4004, and NGC 3310 as given in their Figure 1. Their classification from HyperLeda is Sb, IB, and SABb, respectively. In the plane $\mu_{0,k} - n$, both KIG 685 and KIG 895 (full stars) are located in the very narrow strip of merger remnants.

In summary, both galaxies show signatures of interaction. This is supported by the faint ring-/shell-like residuals in the confirmed iETGs, KIG 685—our *less-isolated* target, and are manifest in the irregular arm structure of the "unconfirmed iETG" and "very isolated" spiral KIG 895.

5 | SUMMARY AND CONCLUSIONS

During two runs of the commissioning phase of the `ARGOS+LUCI` adaptive optic system at `LBT`, we observed two candidate iETGs, namely, KIG 685 and KIG 895, in the K-band, the latter of which had an uncertain classification.

We exploited the best instrumental performance, which reaches ≈0.25" PSF-FWHM, discarding from the stack of images those for which the loop turned from closed to open, degrading the PSF by a factor between 2 and 3 ($0.4''$–$0.6''$).

These two galaxies compose a small picture of what can be done with `ARGOS+LUCI` high-resolution observations, allowing both the detection of fine structure in iETGs and the cleaning of the sample of misclassifications.

This is indeed the main result of the present observations and analysis: both KIG 685 and KIG 895 present "scars," still visible in their structure, of their past interaction/accretion history. KIG 685 is an S0 showing faint ring-/shell-like residuals once a model composed of a pseudobulge plus a disk has been subtracted. We suggest that this is the results of an interaction/accretion event rather than the effect of a gentler secular evolution. KIG 895 is a misclassified early-type. It is a gas-rich, late-type galaxy with an irregular arm structure, likely the result of a recent interaction/accretion, superposed on a nearly pure disk.

A statistically significant sample, cleaned of misclassified objects, is needed to understand the evolutionary history of bona fide iETGs located in such unusually poor environments for this family of galaxies.

REFERENCES

Andreon, S. 2002, *A&A*, *382*, 495.

Annibali, F., Bressan, A., Rampazzo, R., Zeilinger, W. W., & Danese, L. 2007, *A&A*, *463*, 455.

Argudo-Fernández, M., Verley, S., Bergond, G., et al. 2013, *A&A*, *560*, A9.

Bender, R., Surma, P., Doebereiner, S., Moellenhoff, C., & Madejsky, R. 1989, *A&A*, *217*, 35.

Bressan, A., Panuzzo, P., Buson, L., et al. 2006, *ApJ*, *639*, L55.

Buta, R., Laurikainen, E., Salo, H., & Knapen, J. H. 2010, *ApJ*, *721*, 259.

Buta, R. J., Sheth, K., Athanassoula, E., et al. 2015, *Astrophys. J. Suppl. Ser.*, *217*, 32.

Buta, R. J., Verdes-Montenegro, L., Damas-Segovia, A., et al. 2019, *MNRAS*, *488*, 2175.

Capaccioli, M., Caon, N., & Rampazzo, R. 1990, *MNRAS*, *242*, 24.

Cappellari, M. 2016, *Ann. Rev. Astron. Astrophys.*, *54*, 597.

Cattapan, A., Spavone, M., Iodice, E., et al. 2019, *ApJ*, *874*, 130.

Chang, R., Gallazzi, A., Kauffmann, G., Charlot, S., Ivezić, Ž., Brinchmann, J., & Heckman, T. M. 2006, *MNRAS*, *366*, 717.

Ciambur, B. C. 2016, *Publ. Astron. Soc. Aust.*, *33*, e062.

Clemens, M. S., Bressan, A., Nikolic, B., Alexand er, P., Annibali, F., & Rampazzo, R. 2006, *MNRAS*, *370*, 702.

Clemens, M. S., Bressan, A., Nikolic, B., & Rampazzo, R. 2009, *MNRAS*, *392*, L35.

Côté, P., Piatek, S., Ferrarese, L., et al. 2006, *Astrophys. J. Suppl. Ser.*, *165*, 57.

Dressler, A. 1980, *ApJ*, *236*, 351.

Duc, P.-A., Cuillandre, J.-C., Serra, P., et al. 2011, *MNRAS*, *417*, 863.

Duc, P.-A., Cuillandre, J.-C., Karabal, E., et al. 2015, *MNRAS*, *446*, 120.

Dupraz, C., & Combes, F. 1986, *A&A*, *166*, 53.

Dupraz, C., & Combes, F. 1987, *A&A*, *185*, L1.

Eliche-Moral, M. C., Rodríguez-Pérez, C., Borlaff, A., Querejeta, M., & Tapia, T. 2018, *A&A*, *617*, A113.

Fernández Lorenzo, M., Sulentic, J., Verdes-Montenegro, L., Ruiz, J. E., Sabater, J., & Sánchez, S. 2012, *A&A*, *540*, A47.

Fernández Lorenzo, M., Sulentic, J., Verdes-Montenegro, L., et al. 2014, *ApJ*, *788*, L39.

Hill, J. M., Green, R. F., Slagle, J. H., et al. 2008, *The Large Binocular Telescope. Ground-based and Airborne Telescopes II*, eds. L. M. Stepp & R. Gilmozzi, Proceedings of the SPIE, Vol. *7012*, 701203.

Ho, L. C., Li, Z.-Y., Barth, A. J., Seigar, M. S., & Peng, C. Y. 2011, *Astrophys. J. Suppl. Ser.*, *197*, 21.

Huang, S., Ho, L. C., Peng, C. Y., Li, Z.-Y., & Barth, A. J. 2013, *ApJ*, *766*, 47.

Jedrzejewski, R. I. 1987, *MNRAS*, *226*, 747.

Jones, L. R., Ponman, T. J., Horton, A., Babul, A., Ebeling, H., & Burke, D. J. 2003, *MNRAS*, *343*, 627.

Jones, M. G., Espada, D., Verdes-Montenegro, L., et al. 2018, *A&A*, *609*, A17.

Karachentseva, V. E. 1973, *Soobshcheniya Spetsial'noj Astrofizicheskoj Observatorii*, *8*, 3.

Khochfar, S., Emsellem, E., Serra, P., et al. 2011, *MNRAS*, *417*, 845.

Kormendy, J., Fisher, D. B., Cornell, M. E., & Bender, R. 2009, *Astrophys. J. Suppl. Ser.*, *182*, 216.

La Barbera, F., de Carvalho, R. R., de La Rosa, I. G., Lopes, P. A. A., Kohl-Moreira, J. L., & Capelato, H. V. 2010, *MNRAS*, *408*, 1313.

Lauer, T. R. 2012, *ApJ*, *759*, 64. https://doi.org/10.1088/0004-637X/759/1/64.

Lauer, T. R., Faber, S. M., Holtzman, J. A., et al. 1991, *ApJ*, *369*, L41.

Lauer, T. R., Faber, S. M., Currie, D. G., et al. 1992, *AJ*, *104*, 552. https://doi.org/10.1086/116254.

Lauer, T. R., Gebhardt, K., Richstone, D., et al. 2002, *AJ*, *124*, 1975.

Laurikainen, E., Salo, H., Buta, R., Knapen, J. H., & Comerón, S. 2010, *MNRAS*, *405*, 1089.

Laurikainen, E., Salo, H., Buta, R., & Knapen, J. H. 2011, *MNRAS*, *418*, 1452.

Li, Z.-Y., Ho, L. C., Barth, A. J., & Peng, C. Y. 2011, *Astrophys. J. Suppl. Ser.*, *197*, 22.

Lisenfeld, U., Verdes-Montenegro, L., Sulentic, J., et al. 2007, *A&A*, *462*, 507.

Lisenfeld, U., Espada, D., Verdes-Montenegro, L., et al. 2011, *A&A*, *534*, A102.

Longhetti, M., Bressan, A., Chiosi, C., & Rampazzo, R. 1999, *A&A*, *345*, 419.

Malin, D. F., & Carter, D. 1983, *ApJ*, *274*, 534.

Mapelli, M., Rampazzo, R., & Marino, A. 2015, *A&A*, *575*, A16.

Marino, A., Bianchi, L., Rampazzo, R., Thilker, D., Annibali, F., Bressan, A., & Buson, L. M. 2011a, *Ap&SS*, *335*, 243.

Marino, A., Rampazzo, R., Bianchi, L., et al. 2011b, *MNRAS*, *411*, 311.

Marino, A., Mazzei, P., Rampazzo, R., & Bianchi, L. 2016, *MNRAS*, *459*, 2212.

Marquardt, W. D. 1963, *J. Soc. Ind. Appl. Math.*, *11*, 431.

Martin, D. C., Fanson, J., Schiminovich, D., et al. 2005, *ApJ*, *619*, L1.

Mazzei, P., Marino, A., Rampazzo, R., Galletta, G., & Bettoni, D. 2014a, *Adv. Space Res.*, *53*, 950.

Mazzei, P., Marino, A., & Rampazzo, R. 2014b, *ApJ*, *782*, 53.

Mazzei, P., Rampazzo, R., Marino, A., Trinchieri, G., Uslenghi, M., & Wolter, A. 2019, *ApJ*, *885*, 165.

Meert, A., Vikram, V., & Bernardi, M. 2015, *MNRAS*, *446*, 3943.

Morales, G., Martínez-Delgado, D., Grebel, E. K., Cooper, A. P., Javanmardi, B., & Miskolczi, A. 2018, *A&A*, *614*, A143.

Morrissey, P., Conrow, T., Barlow, T. A., et al. 2007, *ApJS*, *173*, 682.

Orban de Xivry, G., Rabien, S., Busoni, L. et al. 2016, First on-sky results with ARGOS at LBT. Adaptive Optics Systems V Vol. *9909*, p. 990936.

Panuzzo, P., Vega, O., Bressan, A., et al. 2007, *ApJ*, *656*, 206.

Panuzzo, P., Rampazzo, R., Bressan, A., et al. 2011, *A&A*, *528*, A10.

Peng, C. Y., Ho, L. C., Impey, C. D., & Rix, H.-W. 2010, *AJ*, *139*, 2097.

Rabien, S., Angel, R., Barl, L., et al. 2019, *A&A*, *621*, A4.

Rampazzo, R., Marino, A., Tantalo, R., et al. 2007, *MNRAS*, *381*, 245.

Rampazzo, R., Panuzzo, P., Vega, O., Marino, A., Bressan, A., & Clemens, M. S. 2013, *MNRAS*, *432*, 374.

Rampazzo, R., Vega, O., Bressan, A., Clemens, M. S., Marino, A., & Panuzzo, P. 2014, *A&A*, *565*, A50.

Rampazzo, R., D'Onofrio, M., Zaggia, S., et al. 2016, in: *From the Realm of the Nebulae to Populations of Galaxies*, eds. M. D'Onofrio, R. Rampazzo, & S. Zaggia, Switzerland: Springer, Vol. *435*, 381.

Rampazzo, R., Mazzei, P., Marino, A., Uslenghi, M., Trinchieri, G., & Wolter, A. 2017, *A&A*, *602*, A97.

Rampazzo, R., Mazzei, P., Marino, A., et al. 2018, *Ap&SS*, *363*, 80.

Rothberg, B., & Joseph, R. D. 2004, *AJ*, *128*, 2098.

Salim, S., & Rich, R. M. 2010, *ApJ*, *714*, L290.

Salo, H., Laurikainen, E., Laine, J., et al. 2015, *Astrophys. J. Suppl. Ser.*, *219*, 4.

Sandin, C. 2014, *A&A*, *567*, A97.

Sandin, C. 2015, *A&A*, *577*, A106.

Seifert, W., Appenzeller, I., Baumeister, H., et al. 2003, in: *Instrument Design and Performance for Optical/Infrared Ground-Based Telescopes*, eds. M. Iye & A. F. M. Moorwood, Proceedings of the SPIE, Vol. *4841*, 962.

Serra, P., Oosterloo, T., Morganti, R., et al. 2012, *MNRAS*, *422*, 1835.

Sérsic, J. L. 1963, *Boletin de la Asociacion Argentina de Astronomia La Plata Argentina*, *6*, 41.

Spavone, M., Iodice, E., Capaccioli, M., et al. 2018, *ApJ*, *864*, 149.

Sulentic, J. W., Verdes-Montenegro, L., Bergond, G., et al. 2006, *A&A*, *449*, 937.

Thilker, D. A., Bianchi, L., Schiminovich, D., et al. 2010, *ApJ*, *714*, L171.

Trujillo, I., & Fliri, J. 2016, *ApJ*, *823*(2), 123.

Trujillo, I., Aguerri, J. A. L., Cepa, J., & Gutiérrez, C. M. 2001, *MNRAS*, *328*, 977.

Turner, M. L., Côté, P., Ferrarese, L., et al. 2012, *The Astrophysical Journal Supplement Series*, *203*, 5.

de Vaucouleurs, G. 1953, *MNRAS*, *113*, 134.

Vega, O., Bressan, A., Panuzzo, P., et al. 2010, *ApJ*, *721*, 1090.

Verdes-Montenegro, L., Sulentic, J., Lisenfeld, U., et al. 2005, *A&A*, *436*, 443.

Verley, S., Leon, S., Verdes-Montenegro, L., et al. 2007a, *A&A*, *472*, 121.

Verley, S., Odewahn, S. C., Verdes-Montenegro, L., et al. 2007b, *A&A*, *470*, 505.

Weil, M. L., & Hernquist, L. 1993, *ApJ*, *405*, 142.